Draft version September 22, 2026
Typeset using LaTeX twocolumn style in AASTeX7.0.1

Star Formation and Nebular Attenuation from Paα, Brα, and Brβ in Massive Dust-obscured Galaxies at Cosmic Noon using JWST

Virginia Vanicek ,[1,2,3] Jed McKinney ,[1,2,*] Alexandra Pope ,[4] Anna Sajina ,[5] Stacey Alberts ,[6] Meredith Stone ,[7] Lee Armus ,[8] Sinclaire M. Manning ,[4] Olivia Cooper ,[9] Tanio Díaz-Santos ,[10] Miriam Eleazer ,[4] Caitlin M. Casey ,[11] Thomas S.-Y. Lai ,[8] Steven L. Finkelstein ,[1,2] Leonid Sajkov ,[12,13] Allison Kirkpatrick ,[14] and Anthony Taylor [1,2]

[1]Department of Astronomy, The University of Texas at Austin, 2515 Speedway Boulevard, Austin, TX 78712, USA
[2]Cosmic Frontier Center, The University of Texas at Austin, Austin, TX 78712
[3]Department of Astronomy, University of Maryland, College Park, MD 20742, USA
[4]Department of Astronomy, University of Massachusetts, Amherst, MA 01003, USA
[5]Department of Physics and Astronomy, Tufts University, Medford, MA 02155, USA
[6]AURA for the European Space Agency (ESA), Space Telescope Science Institute, 3700 San Martin Dr., Baltimore, MD 21218, USA
[7]Steward Observatory, University of Arizona, 933 North Cherry Avenue, Tuscon, AZ 85721, USA
[8]IPAC, California Institute of Technology, 1200 E. California Blvd., Pasadena, CA 91125, USA
[9]Department for Astrophysical & Planetary Science, University of Colorado, Boulder, CO 80309, USA
[10]Institutes of Computer Science and Astrophysics, Foundation for Research and Technology Hellas (FORTH), 100 Nikolaou Plastira str., Vassilika Vouton, Heraklion, 70013, Greece
[11]Department of Physics, University of California Santa Barbara, Santa Barbara, CA, USA
[12]Kavli Institute for Particle Astrophysics and Cosmology, Stanford University, 452 Lomita Mall, Stanford, CA 94305
[13]Department of Physics, Stanford University, 382 Via Pueblo Mall, Stanford, CA 94305
[14]Department of Physics & Astronomy, University of Kansas, Lawrence, KS 66045, USA

ABSTRACT

Near-infrared hydrogen recombination lines can provide robust star-formation rates if the effects of dust attenuation continue to diminish towards longer wavelengths. To quantify near-infrared attenuation and ultimately measure accurate star-formation rates (SFRs) at the height of cosmic star-formation, we present Paα, Brα, and Brβ detections in 27 luminous infrared galaxies at $z \sim 1-2$, including pure star-forming galaxies as well as dust-obscure Active Galactic Nuclei (AGN). Using combined spectra from the JWST MIRI (Mid-Infrared Instrument) LRS (Low Resolution Spectrometer) and the Spitzer Space Telescope IRS we quantify the star formation rates of our sample using a sub-sample of 13 galaxies detected in Paα emission (1.87μm), 14 galaxies detected in Brα (4.05μm), and 12 galaxies detected in Brβ (2.63μm). By combining multiple near-infrared recombination lines in individual galaxies we calculate nebular attenuation, finding $A_\lambda \sim 3$ mag at $\sim 2\,\mu$m and $A_\lambda \sim 1$ mag at $\sim 4\,\mu$m. Nebular lines trace the SFR on ~ 10 Myr timescales, which we compare to the total infrared luminosity ($L_{\rm IR}$) which probes the star formation over the last ~ 100 Myr. SFRs measured from $L_{\rm IR}$ using common conversions are systematically higher than the SFRs derived from attenuation-corrected nebular line measurements by a factor of ~ 2.5. This could be indicative of a declining or static star formation history with a past burst or systematic effects on SFR$_{\rm IR}$ such as dust heating from evolved stellar populations, and/or an active galactic nucleus.

Keywords: Galaxies (573) — Cosmology (343) — Interstellar medium (847)

1. INTRODUCTION

Nearly 10 billion years ago ($z \sim 2$) galaxies were forming more stars and growing their supermassive black holes more rapidly than at any other time in the Universe. This is observed as a peak in the star formation rate density (SFRD, P. Madau & M. Dickinson 2014; J. A. Zavala et al. 2021) and black hole accretion rate density (BHARD, P. Madau & M. Dickinson 2014; S. J. Kim et al. 2024; A. J. Porras-Valverde et al. 2026). Dur-

* NASA Hubble Fellow

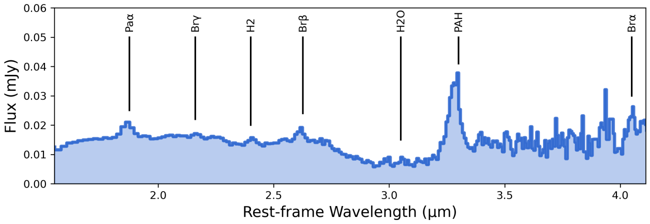

Figure 1. JWST MIRI/LRS spectra of GN-IRS-7 ($\lambda_{\rm obs} = 5-14\mu$m) at $z_{spec} = 1.998$, the only galaxy in our sample with the wavelength coverage in JWST to have Paα, Brα, and Brβ emission lines. Due to the noise at Brα, it fails our SNR > 3 cut. We use the observed line fluxes from these hydrogen recombination lines throughout the sample to measure dust attenuation in the individual galaxies.

ing this time, dusty luminous infrared galaxies (LIRGs, $L_{\rm IR} \equiv 10^{11}-10^{12} L_\odot$) and ultra luminous infrared galaxies (ULIRGs, $L_{\rm IR} \equiv 10^{12}-10^{13} L_\odot$) dominate the SFRD (J. A. Zavala et al. 2021).

Star-formation rates (SFRs) in heavily dust-attenuated galaxies are best measured in the mid-infrared where the effects of dust attenuation on hydrogen recombination lines are minimal (e.g., S. Alberts et al. 2026) and thermal emission from dust heated by starlight can be observed directly (R. C. Kennicutt 1998; D. Calzetti 2013), or in the radio from extinction-independent free-free emission (E. J. Murphy et al. 2011). These different star-formation rate indicators have their own benefits and drawbacks, and probe the star-formation rate averaged over different timescales. For instance, hydrogen recombination lines trace H II regions photoionized by O stars with lifetimes on timescales of ~ 10 Myr (P. Madau & M. Dickinson 2014). Dust attenuation corrections are needed for accurate SFRs derived from hydrogen lines, even in the near-infrared, owing to non-negligible opacities (B. Lo Faro et al. 2017; N. A. Reddy et al. 2020, 2026; M. A. Wozniak et al. 2026). The integrated $\lambda_{\rm rest} = 8-1000\,\mu$m infrared luminosity ($L_{\rm IR}$) traces the SFR averaged over ~ 100 Myr and is more robust against attenuation effects, but can suffer from degenerate heating effects by old stellar populations and supermassive black holes (C. C. Hayward et al. 2014; J. McKinney et al. 2021; J. Bardati et al. 2026). Collecting multiple SFR diagnostics in galaxies is one way to mitigate these systematic uncertainties (e.g., E. J. Murphy et al. 2011). This has been historically challenging for dust-obscured galaxies due to high rest-frame optical attenuation (C. M. Casey et al. 2014b). Thanks to its sensitivity, JWST can now access these features in galaxies with high $V-$band attenuation ($A_V \gtrsim 1$, e.g., O. R. Cooper et al. 2025), and can reach rest-frame near-infrared recombination lines owing to its wavelength coverage (C. Neufeld et al. 2024; S. Alberts et al. 2026).

In this work, we use the JWST Mid-Infrared Instrument (MIRI) Low Resolution Spectrometer (LRS) to measure SFRs and near-infrared attenuation in a sample of 27 massive, infrared-luminous galaxies ($L_{\rm IR}/L_\odot \sim 10^{11}-10^{13}$) at $z = 0.6-2.2$ from J. McKinney et al. (2026). This sample includes pure star-forming galaxies, heavily obscured Active Galactic Nuclei (AGN), and composites. We compare SFRs from Paschen α (Paα), Brackett α (Brα), and Brackett β (Brβ) to IR-derived SFRs to characterize nebular attenuation and SFRs at different timescales in the most actively star-forming galaxies at cosmic noon ($z \sim 1-3$).

Section 2 summarizes the sample selection and data reduction from J. McKinney et al. (2026). In Section 3 we describe our analysis of the Paα, Brα, and Brβ emission lines used to measure SFRs and near-IR dust attenuation. In Section 4 we discuss and compare these SFRs to each other, and we summarize our findings in Section 5. Throughout this paper we assume a Chabrier Initial Mass Function (IMF) (G. Chabrier 2003) and adopt a standard cosmology of $\Omega_\Lambda = 0.7$, $\Omega_M = 0.3$, and $H_0 = 70$ km s^{-1} Mpc^{-1}. All magnitudes correspond to the AB magnitude system (J. B. Oke 1974).

2. DATA

2.1. *Sample Selection*

In this work we analyze a subset of galaxies with MIRI LRS spectra from the JWST Cycle 2 Program #3224 (PI: McKinney). The JWST data used in this paper can be found in the Mikulski Archive for Space Telescopes (MAST): 10.17909/18v0-8068. The survey design, strategy, and data reduction are described in J. McKinney et al. (2026). In summary, JWST PID #3224 targeted 37 dusty galaxies with redshifts $0.6 < z < 2.2$ and stellar masses $10^{10}-10^{11.5} M_\odot$ using the JWST MIRI Low Resolution Spectrometer (LRS) in combination with archival Spitzer IRS spectra to cover an observed wavelength range of $\lambda_{\rm obs} = 5-38\mu$m. These galaxies span a range of AGN contribution from pure dust-obscured star-forming galaxies to highly obscured AGN. The AGN contribution is quantified by $f_{\rm AGN}$, the fraction of light in the mid-IR ($\lambda_{rest} \sim 5-12\mu$m) attributed to thermal dust emission from a hot dusty torus around the AGN, which is accurate to 10% (A. Pope et al. 2008; A. Kirkpatrick et al. 2015). This sample was selected from a parent sample of 343 LIRGs described in A. Kirkpatrick et al. (2012) and we utilize the $f_{\rm AGN}$ measurements made in A. Kirkpatrick et al. (2012, 2015, 2017). The JWST data reduction of the sample is discussed in detail in J. McKinney et al. (2026). As a

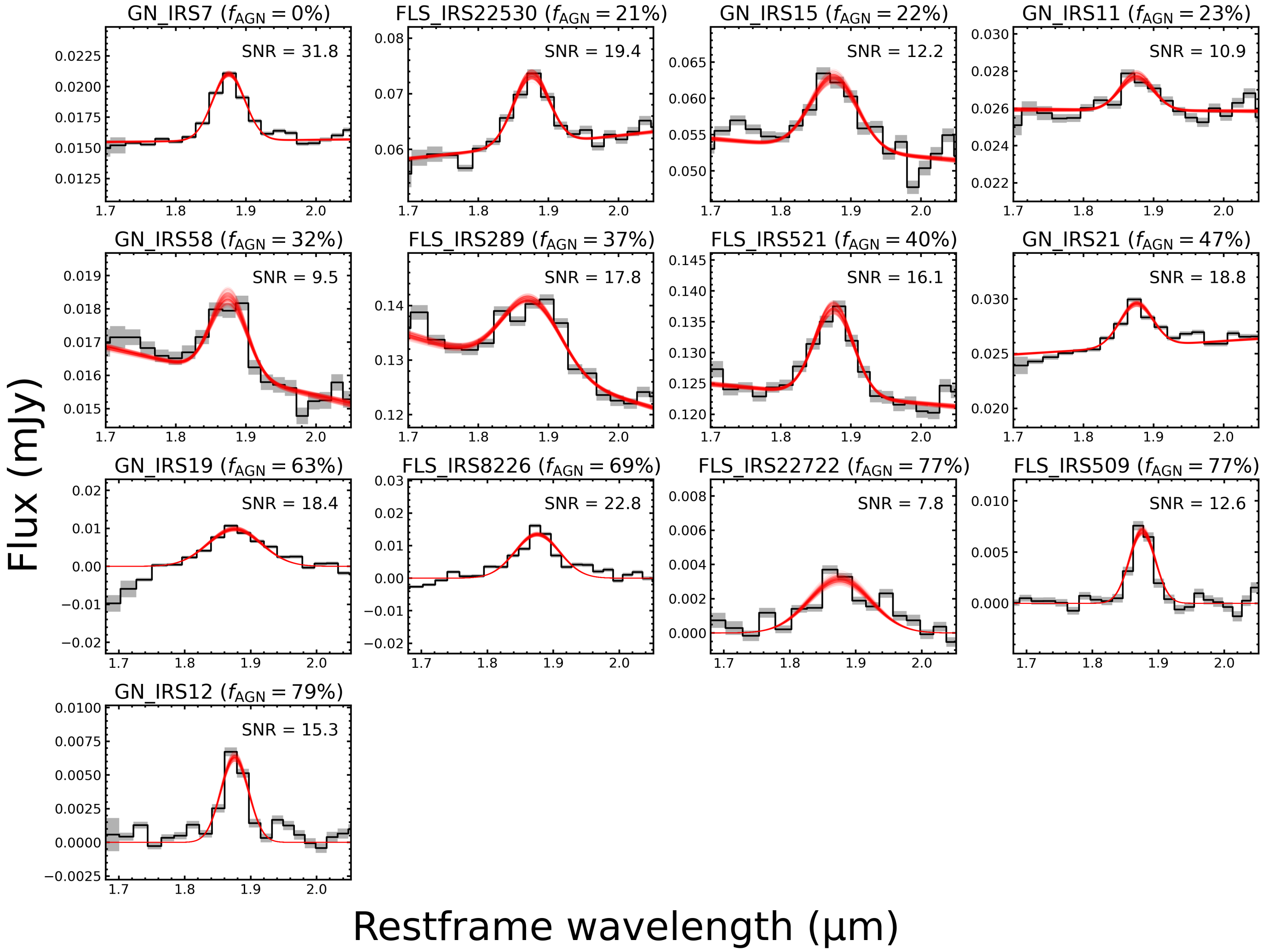

Figure 2. Paα `emcee` fits for our subsample of galaxies that have SNR > 3 Paα detections, ordered by the fraction of mid-infrared emission attributed to a dust-obscured AGN ($f_{\rm AGN}$). The observed spectra are in black, and have been continuum-subtracted in sources with $f_{\rm AGN} > 60\%$ for clarity due to the steeply-rising near-IR continuum Paα sits on top of. The `emcee` modeled emission are the red gaussian lines showing the top 10% of fits. These fits incorporate both the line spread function of JWST MIRI and are resampled to the spectral resolution of LRS.

brief summary, the sample is reduced using the JWST pipeline (version 1.15.1, H. Bushouse et al. 2025) with custom background subtraction in place of the standard Stage 3 routines. 1D spectra are extracted from the background-subtracted 2D spectra using a custom PSF-weighted aperture for each source, and are then normalized to Spitzer IRAC photometry and IRS spectroscopy.

From the parent sample of 37 galaxies from J. McKinney et al. (2026) we select all sources with a significant (signal-to-noise ratio, SNR>3) Paα (1.87μm), Brα (4.05μm), or Brβ (2.63μm) emission line. The number of galaxies in each subsample and their redshift, stellar mass, and $f_{\rm AGN}$ are described in Table 1.

Due to the wavelength coverage of MIRI LRS ($\lambda_{\rm obs} = 5-14\mu$m), the Pa$\alpha$ subset consists of the galaxies in the parent sample with the highest redshifts. The sample of Brα emitting galaxies span a relatively smaller redshift range. At higher redshifts, Brα falls in Spitzer IRS and cannot be detected due to the limited sensitivity and resolving power of those data. The Paα and Brβ subsamples span a larger range in $f_{\rm AGN}$ than the subset of

Table 1. Properties of the Paα, Brα, and Brβ sub-samples.

Sample	Amount	Redshift	$\log(M_*/M_\odot)$	$f_{\rm AGN}$
Paα	13	$1.8-2.2$	$10.1-11.6$	$0-79\%$
Brα	14	$0.6-1.5$	$10.2-11.5$	$0-38\%$
Brβ	12	$1.2-2.1$	$10.7-11.6$	$0-79\%$

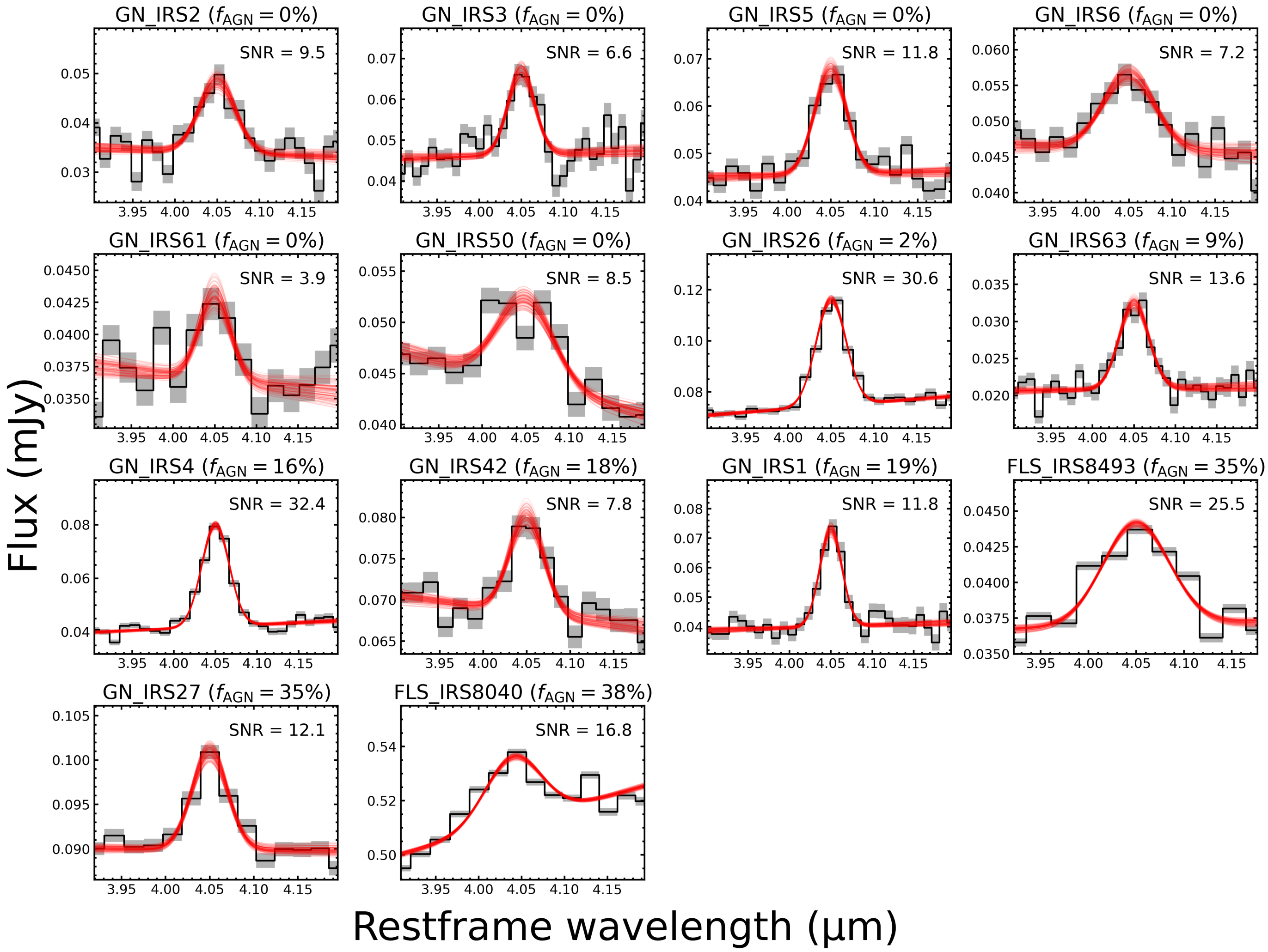

Figure 3. Brα `emcee` fits for our subsample of galaxies that have a SNR $>$ 3 Brα detection in order of $f_{\rm AGN}$. The observed spectra are in black. The `emcee` modeled emission are the red gaussian lines showing the top 10% of fits. These fits incorporate both the line spread function of JWST MIRI and the spectral resolution of LRS.

sources detected in Brα. This arises from the original selection criterion of the parent sample tied to Spitzer MIPS 24 μm fluxes, which combined with the redshifting of the Paα line and the blue edge of LRS, preferentially selects the more luminous galaxies at $z > 1.65$ which are more likely to harbor a dust-obscured AGN (A. Kirkpatrick et al. 2015). Nevertheless, star-formation dominated galaxies with $f_{\rm AGN} < 30\%$ are represented in each sub-sample. Only one galaxy (GN-IRS-7, shown in Figure 1) sits at a redshift of $z = 1.998$ wherein Paα, Brα, and Brβ fall within the LRS wavelength coverage but the Brα emission has a much lower SNR than the other two lines due to the declining sensitivity of LRS beyond $\sim 13\,\mu$m.

3. ANALYSIS

3.1. *Total Stellar Mass*

We fit all sources in the sample using the spectral energy distribution (SED) fitting code `CIGALE` (M. Boquien et al. 2019), assuming a double-exponential SFH with $\tau_{\rm main} \in [0.1, 3]$ Gyr and $\tau_{\rm burst} \in [-0.3, 0.01]$ Gyr. We model an AGN component using the `SKIRTOR` model library (M. Stalevski et al. 2016), and the IR SED using the combined modified blackbody and mid-IR power law model from C. M. Casey et al. (2012). These fits make use of near- through far-infrared photometry from $\sim 1 - 500\,\mu$m, including J- and K-band photometry from VLT/ISAAC (J. Retzlaff et al. 2010), Spitzer IRAC $3.6, 4.5, 5.8, 8.0\mu$m, MIPS 24μm; Herschel PACS $70, 100, 160\mu$m and SPIRE $250, 350, 500\mu$m (A. Kirkpatrick et al. 2015). We find no systematic offset between the stellar masses estimated this way and those

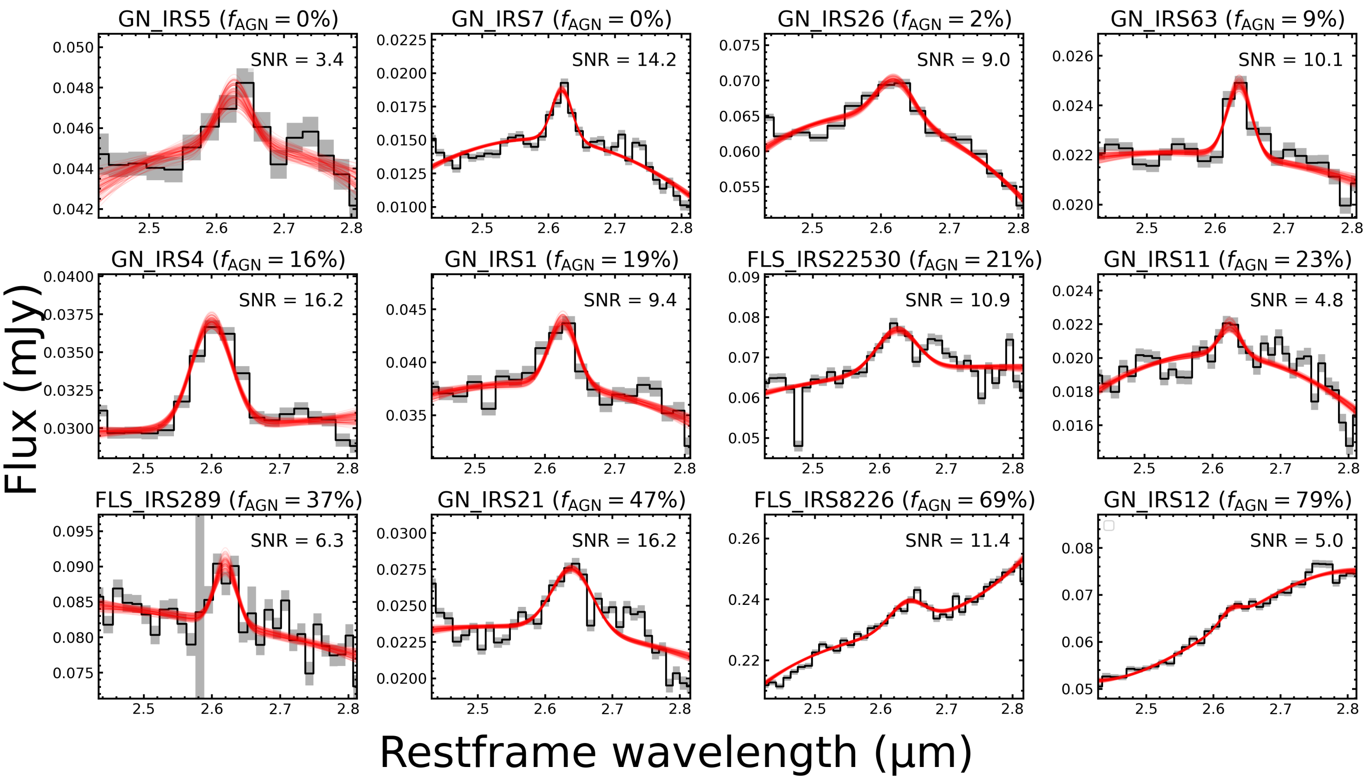

Figure 4. Brβ `emcee` fits for our subsample of galaxies that have a SNR > 3 Brβ detection in order of f_{AGN}. The observed spectra are in black. The `emcee` modeled emission are the red gaussian lines showing the top 10% of fits. These fits incorporate both the line spread function of JWST MIRI and the spectral resolution of LRS.

from prior works on the same galaxies (A. Kirkpatrick et al. 2017).

3.2. *Emission Line Modeling*

To measure SFRs from the hydrogen recombination lines, we fit Paα, Brα, and Brβ using `emcee` (D. Foreman-Mackey et al. 2013), an affine invariant Markov Chain Monte Carlo ensemble sampler. We fix the redshift and line center of each source based on the redshifts measured in J. McKinney et al. (2026) from the Paα and Brα emission lines. We model the lines as a 1D Gaussian with a linear or polynomial continuum, dependent on the effect of AGN on the continuum shape. We adopt a 2nd order polynomial continuum for sources with $f_{\mathrm{AGN}} > 65\%$. We restrict to fitting just the local continuum within $\Delta\lambda \approx 0.15\,\mu$m which we found to best capture the continuum behavior with minimal contamination from nearby features. In addition, we account for the effects of the MIRI LRS line spread function by convolving model spectra with a Gaussian kernel where the width is determined from the P750L spectral resolving power using the wavelength-dependent dispersion and resolution, as obtained from the JWST Pandeia reference data system (TRDS) v5.1. Finally, models are re-gridded to the LRS wavelength resolution using a flux-conserving resampling algorithm implemented in `specutils` (Astropy Collaboration 2026). We note that this fitting method works particularly well for Paα and Brα due to the well-behaved local linear continuum. The continuum around Brβ is much more complicated. Brβ is between two absorption features (as can be seen in Figure 1) caused by stellar atmospheres and dense gas and dust making the continuum non-linear in many instances (see Figure 4). We fit the continuum around Brβ with a 2nd order polynomial which we found in testing to preform the best continuum characterization upon visual inspection. For sources with $f_{\mathrm{AGN}} > 60\%$ we adopt a 3rd order polynomial to account for the absorption features and the steep continuum caused by the AGN. The continuum is well-separated by Brβ in the majority of our spectra, and we note that the precise continuum model does not significantly impact the inferred line luminosities. Note that for sources dominated by AGN ($f_{\mathrm{AGN}} > 60\%$), the emission lines do not appear as prominent as in their star-formation dominated counterparts. This is due to a combination of the aggressive smoothing from the LSF and the steeply-rising power-law nature of the continuum. For visual purposes, we have continuum-subtracted the AGN dominated sources in Fig. 2. Line uncertainties and the subsequent SNR ratios shown on Figures 2 and 3 are taken from the em-

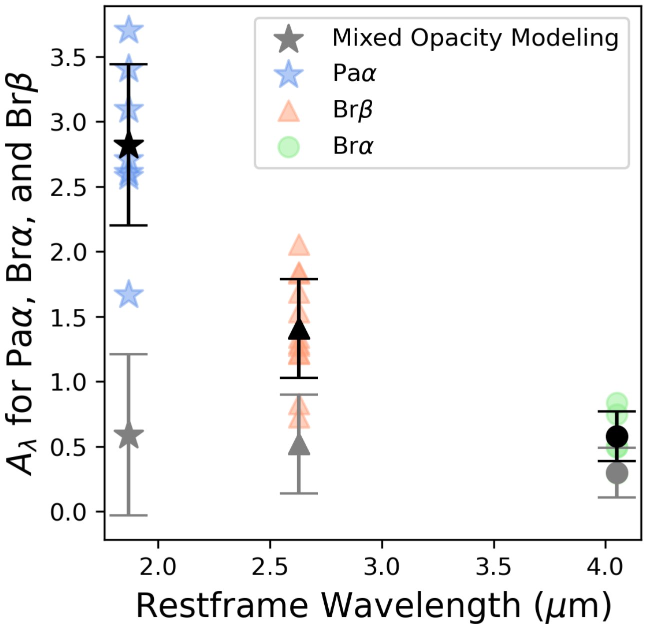

Figure 5. Measured attenuation from $1.8-4.05\mu$m across our sample from galaxies detected in two ore more hydrogen transitions. Paα is denoted by stars, Brβ by triangles, and Brα by circles. The average of the mixed opacity modeling from J. McKinney et al. (2026) is shown in gray which represents the attenuation correction applied to the stellar and dust continuum at these wavelengths. Each individually measured nebular line attenuation is plotted in color with the average of each sub-sample in black. The difference between the continuum and nebular attenuation is ~ 2 magnitudes at Paα, and consistent with one another by Brα at 4.05μm.

pirical spectral noise, which is the dominant error term for Paα and Brα due to the well-behaved continuum. Brβ lines fluxes are dominated by the model uncertainties, which the reported SNRs incorporate.

LRS has a spectral resolution of $R \approx 100$, which means that the emission lines in our targets are not spectroscopically resolved. As a result, we do not have constraint on velocity widths. We therefore restrict line widths to the narrow range of $300 \leq v \leq 500\,\mathrm{km\,s^{-1}}$ as is typical for the observed rotational velocities of galaxies with similar total stellar mass and IR luminosity to our targets (e.g., J. E. Birkin et al. 2024; O. R. Cooper et al. 2025). The best fit models to the Paα, Brα, and Brβ emission lines can be seen in Figure 2, Figure 3, and Figure 4 respectively with each emission line's corresponding SNR.

3.3. *Dust Attenuation*

To correct for the effects of dust attenuation on emission lines measured from the JWST spectra, we begin by considering the opacity curves described in J. McKinney et al. (2026) which were obtained by fitting the LRS spectra with wavelengths of $3-12\mu$m and photometric constraints out to rest-frame 24μm. These opacity curves model all of the dust in the systems as a mixed dust geometry wherein the dust is mixed homogeneously with the emitting medium. The dust extinction profile comes from J. C. Weingartner & B. T. Draine (2001) which assumes Milky Way-like dust (J. A. Cardelli et al. 1989; L. Clarke et al. 2025), that is then scaled to the opacity of the 9.7μm silicate absorption feature of each source to infer the shape of the extinction profile down to short wavelengths. While this is appropriate for deriving dust attenuation corrections to the the Polycyclic Aromatic Hydrocarbon features (e.g., T. S. Y. Lai et al. 2020), which was the focus of J. McKinney et al. (2026), this assumption likely underestimates the attenuation corrections for nebular emission lines tracing young star-forming regions deeply embedded in dust-rich birth clouds (D. Calzetti et al. 2000; S. Charlot & S. M. Fall 2000). In addition, the extinction curves from the J. McKinney et al. (2026) fits in the rest-frame near-IR rely on extrapolations to bluer wavelengths, further adding to their uncertainty.

Hydrogen recombination line ratios can be used to derive a nebular attenuation correction by comparing to the expected ratio for Case B recombination (e.g., N. A. Reddy et al. 2020; N. J. Cleri et al. 2022; M. K. M. Prescott et al. 2022; N. A. Reddy et al. 2023; O. R. Cooper et al. 2025; R. L. Sanders et al. 2025; N. A. Reddy et al. 2026). Naturally, this method requires more than one hydrogen recombination line detection. Our sample includes 7 galaxies with both Paα and Brβ, and 5 galaxies with both Brα and Brβ. We use these to estimate the attenuation impacting the nebular emission lines by first assuming Case B intensity ratios from D. E. Osterbrock & G. J. Ferland (2006) for $T = 10^4K$. We then follow D. Calzetti et al. (2000); S. Wang & X. Chen (2019); N. A. Reddy et al. (2020, 2026). To estimate the $V-$band attenuation we assume an attenuation law of $A_\lambda \propto \lambda^{-\alpha}$ and $\alpha = 2.07 \pm 0.03$ (S. Wang & X. Chen 2019). Our final nebular reddening corrections are insensitive to the choice of α. We measure a mean ($\pm 1\sigma$) attenuation of $A_{\mathrm{Pa}\alpha} = 2.82 \pm 0.61$ mag, $A_{\mathrm{Br}\beta} = 1.4 \pm 0.39$ mag, and $A_{\mathrm{Br}\alpha} = 0.58 \pm 0.19$ mag. As expected, we measure a decrease in the mean attenuation for progressively longer wavelength emission lines (as can be seen in Figure 5). The attenuation at $\lambda_{\mathrm{rest}} = 4.05\,\mu$m remains non-zero with ~ 0.6 mag, similar of the near-infrared attenuation found for local ULIRGs (T. W. Murphy et al. 2001; H. Dannerbauer et al. 2005; L. Armus et al. 2007). Given the extreme obscuration of our sample, even these nebular attenuation measurements may be underestimating the atten-

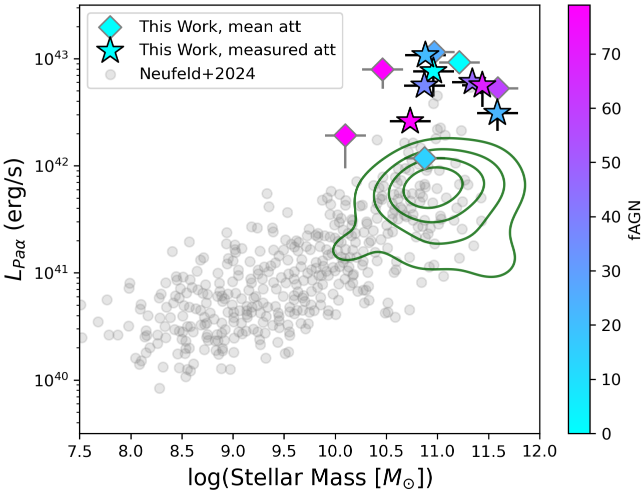

Figure 6. Paα luminosity and stellar mass for galaxies in our sample compared to that of C. Neufeld et al. (2024) (gray circles) which also uses Paα at $z = 1-1.7$ galaxies to measure a SFR. Our galaxies are at the higher mass end of the C. Neufeld et al. (2024) sample and are initially consistent with the higher luminosity sources. After dust correction from our nebular derived attenuation (Section 3.3, where the gray outline points utilize the average attenuation of the sources with multiple hydrogen recombination lines), we find that our sources are within the envelope of the sources from C. Neufeld et al. (2024), but that they reach the high luminosity end of the sample. The green contours show the luminosity distribution of sources without dust correction, indicating that the nebular dust attenuation correction systematically increased Paα luminosities.

uation toward the most deeply embedded star-forming regions in our sources.

From these same galaxies, using the mixed opacity modeling from J. McKinney et al. (2026), the mean ($\pm 1\sigma$) attenuation is $A_{\mathrm{Pa}\alpha} = 0.59 \pm 0.55$, $A_{\mathrm{Br}\beta} = 0.52 \pm 0.39$, and $A_{\mathrm{Br}\alpha} = 0.30 \pm 0.17$. These attenuation values are significantly lower than what we calculate from the nebular lines, by up to a factor of ~ 4.5 at Paα and ~ 2 at Brα. This is seen in Figure 5 which shows the average attenuation from the mixed opacity modeling compared to the measured attenuation from the emission lines and their corresponding average. Paα is the most affected by the new attenuation measurements, and Brα is the least sensitive, consistent with a steeply rising attenuation curve. Overall this trend naturally arises from differential reddening, where the nebular emission from young, obscured H II regions experiences more attenuation than stars mixed in the diffuse ISM. The relative offset between these two attenuation corrections yields an average differential reddening of $\mathrm{E(B-V)_{gas}} - \mathrm{E(B-V)_{ISM}} = 0.70 \pm 0.20, 0.27 \pm 0.12, 0.09 \pm 0.06$ for Paα, Brβ, and Brα respectively, assuming $R_V = 3.1$ (D. Calzetti et al. 2000). This is comparable, particularly with Brα and Brβ, to what is found for the differential reddening between nebular lines and stellar continuum for massive ($M_* > 10^{10}\, M_{\odot}$) $z = 2.7-4$ galaxies with NIRSpec detections of Hα, Hβ, and Hγ (C. Woodrum et al. 2025; S. Karthikeyan et al. 2026). Thus we find that the effects of differential reddening remain significant up to Brα in the most massive, dust-obscured galaxies at cosmic noon, as has been observed in their local counterparts (H. Dannerbauer et al. 2005; L. Armus et al. 2007).

3.4. *Star Formation Rates from Paα, Brα, and Brβ*

We next use the dust-corrected recombination line luminosities to measure star-formation rates. If the galaxy has multiple hydrogen recombination lines, we use the attenuation measured directly for that source as described in Section 3.3. If the target only has one emission line, we use the average attenuation for the corresponding line measured from the rest of the sample (black points in Figure 5). Sources where the nebular attenuation is assumed rather than measured directly are denoted in all figures by a marker with a gray outline (as compared to a black outline). We derive SFRs for Paα, Brα, and Brβ using the calibration of the Hα SFR in R. C. Kennicutt & N. J. Evans (2012). We then use the intrinsic ratios between Hα and Paα, Brα, and Brβ in D. E. Osterbrock & G. J. Ferland (2006), assuming Case B recombination and $T = 10^4$ K to convert the Hα SFR formulation to Paα, Brα, and Brβ. Because we assume a Chabrier IMF, we convert the Kroupa IMF Hα SFR in R. C. Kennicutt & N. J. Evans (2012) through the IMF relation described by E. R. Stanway & J. J. Eldridge (2019). Our final SFR relations are:

$$\mathrm{SFR_{Pa\alpha}}[M_{\odot}/\mathrm{yr}] = 6.9 \times 10^{-41}\, L_{\mathrm{Pa}\alpha}\, [\mathrm{erg\,s^{-1}}] \quad (1)$$

$$\mathrm{SFR_{Br\alpha}}[M_{\odot}/\mathrm{yr}] = 2.9 \times 10^{-40}\, L_{\mathrm{Br}\alpha}\, [\mathrm{erg\,s^{-1}}] \quad (2)$$

$$\mathrm{SFR_{Br\beta}}[M_{\odot}/\mathrm{yr}] = 5.2 \times 10^{-40}\, L_{\mathrm{Br}\beta}\, [\mathrm{erg\,s^{-1}}] \quad (3)$$

We report the resulting SFRs in Table 2. As shown in Figure 7 for sources with multiple hydrogen recombination lines, the measured line SFRs are consistent with each other within the uncertainties for SFRs between $10 - 800 M_{\odot}\mathrm{yr}^{-1}$.

We note that we do not apply an AGN-ionization correction to the recombination line SFRs (e.g., M. Stone et al. 2022). While strong nebular line emission can arise from the narrow line region around the AGN, this effect is mitigated by increasing obscuration (e.g., R. C. Hickox

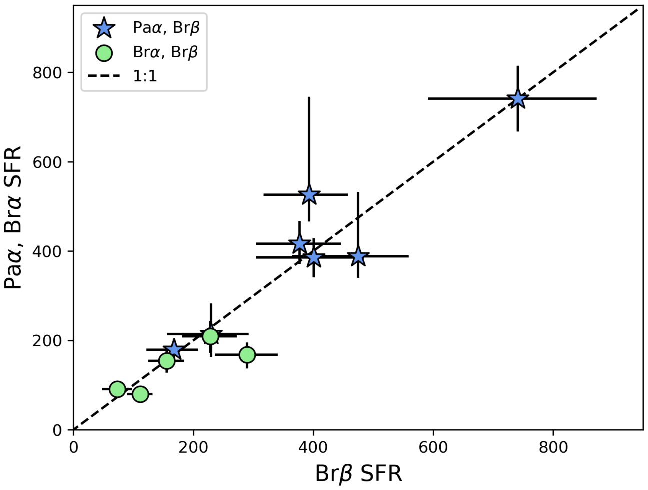

Figure 7. SFR comparison for the galaxies that have multiple hydrogen recombination lines. Galaxies that have both Paα and Brβ are denoted by blue stars while sources with Brα and Brβ are denoted by green circles. There is a very strong correlation between the SFRs measured using Paα, Brα and Brβ which confirms the use of our attenuation models creating consistency between the SFR indicators.

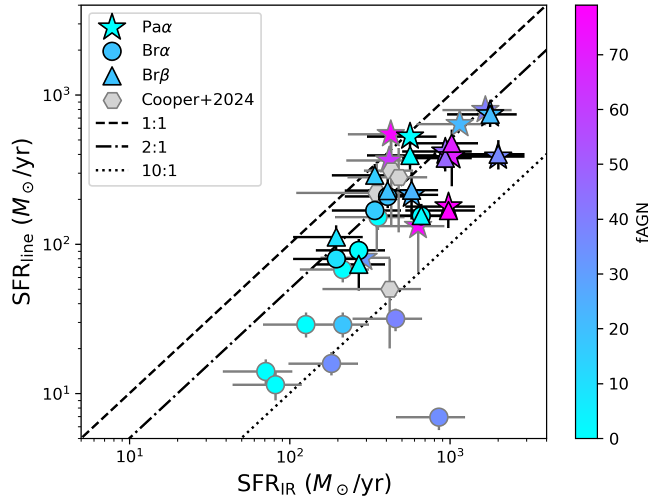

Figure 8. A comparison of the Paα (stars), Brα (circles), Brβ (triangles) SFRs ($\sim$ 10 Myr) and the $L_{\rm IR}$ SFRs ($\sim$ 100 Myr). Sources that had multiple hydrogen recombination lines to measure an individual attenuation have black outlines while the sources that used the mean attenuation for their dust correction have gray outlines. Included are sources from O. R. Cooper et al. (2025) with a similar mass and $L_{\rm IR}$ at $z \sim 2.3-2.7$ which find a similar scatter of SFRs using Hα and the $L_{\rm IR}$. The sample falls between zero and one order of magnitude discrepancy of SFR tracers.

& D. M. Alexander 2018). Indeed, we do not find a trend between the recombination line SFRs and mid-IR AGN fraction, suggesting that the obscured AGN in our sample might not systematically bias the corresponding SFRs high. As a final note, only 5/27 (19%) galaxies in our sample have $f_{\rm AGN} > 50\%$, suggesting that this effect (if present) would not bias interpretations of the sample as a whole.

Due to the longer rest-frame wavelength and relatively fainter line flux of Brα, literature measurements of Brα are historically limited to nearby galaxies where the line is accessible with ground-based IR facilities or AKARI (e.g., D. L. Depoy et al. 1987; S. C. Beck et al. 1989; H. Inami et al. 2018). Here we present the first compilation of Brα SFRs for $z \sim 1-2$ massive, dust-obscured star-forming and AGN dominated galaxies. The SFR$_{\rm Br\alpha}$ are shown in Table 2 and range from $10-150\,M_\odot\,{\rm yr}^{-1}$. As the Pa$\alpha$ and Brβ sample encompass populations with a higher average $L_{\rm IR}$ than Brα, their SFR ranges reach higher values. The SFR$_{\rm Pa\alpha}$ and SFR$_{\rm Br\beta}$ are also shown in Table 2 and range from $80-800\,M_\odot\,{\rm yr}^{-1}$ and $70-750\,M_\odot\,{\rm yr}^{-1}$ respectively.

Figure 6 compares the Paα luminosities we measure to the sample of C. Neufeld et al. (2024) who use NIRspec to detect Paα at $1.0 < z < 1.7$ as part of the FRESCO survey (P. A. Oesch et al. 2023). Without applying any dust corrections, our sample falls along the massive end of the distribution reported in C. Neufeld et al. (2024). Our fiducial dust-corrected Paα luminosities (using measured nebular attenuation factors) are on-average larger for fixed stellar mass than the most massive galaxies in (C. Neufeld et al. 2024). This is expected as our galaxies were selected as a representative sample of some of the brightest dust obscured sources at $z \sim 1-2$ that are also relatively rarer and correspondingly less likely to be found in statistical quantities within < 100 arcmin^2 surveys like FRESCO.

3.5. *Star Formation Rate from the far-IR*

Using the $L_{\rm IR}$ integrated between $8-1000\mu$m measured from Herschel Space Observatory observations in A. Kirkpatrick et al. (2015) we measure SFRs over $\sim$ 100 Myr. The SFRs derived from $L_{\rm IR}$ (hereafter SFR$_{\rm IR}$) were measured following E. J. Murphy et al. (2011) as described in the survey overview paper (J. McKinney et al. 2026).

4. RESULTS AND DISCUSSION

Using the opacity models derived strictly from the mid-IR continuum modeling (J. McKinney et al. 2026), we found that the nebular line derived SFRs were one to two orders of magnitude below SFR$_{\rm IR}$, which we interpret as a significant initial underestimation of the nebular attenuation motivating the analysis described in Section 3.3. Using the attenuation derived from multiple hydrogen recombination lines for the sources that have multiple, and the average for the sources that only have one, we compare the nebular line SFRs to the SFR_{IR} for each source in Figure 8. We continue to see an offset between the two different star formation rate indicators, but now the difference is between zero and one order of magnitude with 25% having SFR_{line} that agree with SFR_{IR} within the errors of both measurements.

Figure 9 compares the monochromatic attenuation inferred from nebular line ratios to the attenuation needed for the observed line flux to reproduce SFR_{IR}. We find that the attenuation needed for SFR_{IR} and SFR_{line} to agree is systematically greater than what we measure directly by a factor of ~ 1 mag. This holds for each line pair, meaning the offset does not disappear when using a more transparent part of the spectrum (i.e., Brα vs. Paα). C. M. Casey et al. (2026a) finds that the A_V inferred from optical/UV continuum underestimates L_{IR} by a factor of ~ 3 across most mass ranges out to high redshift. This is consistent with our findings assuming that the attenuated UV/optical continuum *and* nebular lines from stars do not fully capture on-going star-formation in heavily obscured regions. As discussed in Section 3.3, we find comparable differential reddening between nebular lines and stellar continuum to other spectroscopic studies with well-sampled Balmer series (C. Woodrum et al. 2025; S. Karthikeyan et al. 2026). Therefore, we also consider interpretations including a poorly calibrated and/or contaminated SFR_{IR} measurement, geometric effects, and very dense H II regions.

As noted in C. Neufeld et al. (2024) using NIRCam/grism measurements, Paα can exhibit clumpy morphologies. If the $0.51'' \times 4.7''$ LRS slit does not capture the full extent of a galaxy's nebular line emission, then we could be missing some amount of Paα, Brα, and Brβ flux even after the aperture corrections which were anchored to unresolved Spitzer/IRAC and IRS peak-up photometry (J. McKinney et al. 2026). We find that there is no correlation between the ratio of $SFR_{Pa\alpha,Br\alpha,Br\beta}$ and SFR_{IR} and the slit-loss correction factors derived in J. McKinney et al. (2026) with a Pearson coefficient of 0.034 and p-value of 0.84. It is unlikely that slit losses are contributing to the difference in SFRs; however, we acknowledge that they are presently anchored to the continuum which can exhibit different morphological structure than emission lines maps (C. Neufeld et al. 2024).

Geometric effects are also discussed in O. R. Cooper et al. (2025) who use NIRSpec MSA slitlets to measure Hα across their sample of galaxies of higher redshift than those in this work, but of comparable mass, SFR, and IR luminosity. They note the cold dust emission tracing L_{IR} localized by ALMA is always centered in the MSA slit, indicating that the offset between star-formation rate indicators is likely not driven by missing far-infrared flux outside of the slit. Additional resolved imaging could directly constrain the role of star-formation geometry and clumpy morphologies in our sample. Changes in dust-to-star geometries naturally allow for different emergent attenuation laws (G. L. Granato et al. 2000; D. Calzetti et al. 2000).

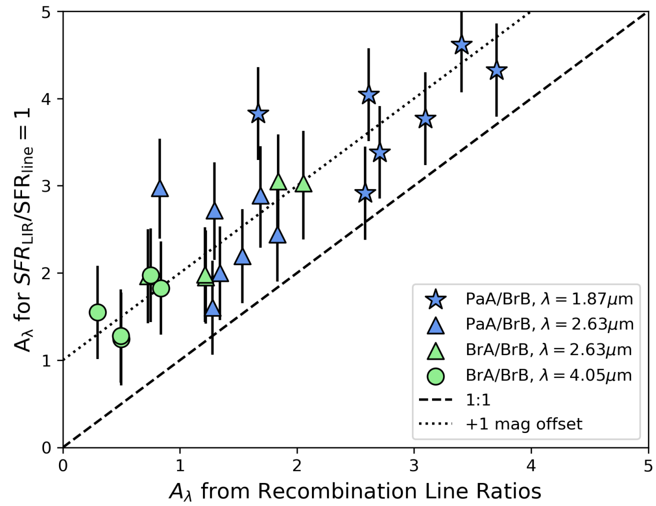

Figure 9. Nebular attenuation derived from the hydrogen recombination lines compared to the amount of attenuation needed to increase the SFRs derived from the emission lines to be the same as the SFRs from the L_{IR} in terms of an attenuation correction factor. The shapes correlate to the SFR used on the y-axis while the colors correlate to the two lines used in the attenuation derivation. We find a systematic offset compared to the 1 mag offset of the y-axis in orange, of our sample with only two sources having an attenuation that puts the recombination SFRs at the same value of SFR_{IR}.

It is also possible that SFR_{IR} is over-estimated. From a theoretical perspective, AGN heating and older stellar populations can bias L_{IR} SFRs high by providing energy from a source unassociated with the UV output of $\sim 10 - 100$ Myr-averaged star formation. As shown in J. McKinney et al. (2021) and J. Bardati et al. (2026) using post-processed radiative transfer simulations, dust-enshrouded AGN can power significant cold dust emission such that L_{IR} can be increased by an order of magnitude by reprocessed AGN photons alone. C. C. Hayward et al. (2014) use similar simulation methods to show that L_{IR} can also be boosted by dust heating from evolved stars having formed > 100 Myr before a burst. Indeed, the largest disagreement between SFR_{IR} and $SFR_{H\alpha}$ observed in the star-forming sample of O. R. Cooper et al. (2025) is associated with the strongest Balmer break and oldest stellar age. Our well-sampled mid-IR spectroscopy mitigates the effects of AGN heating of dust by providing a handle on subtracting out the AGN component of far-IR emission (e.g., A. Pope

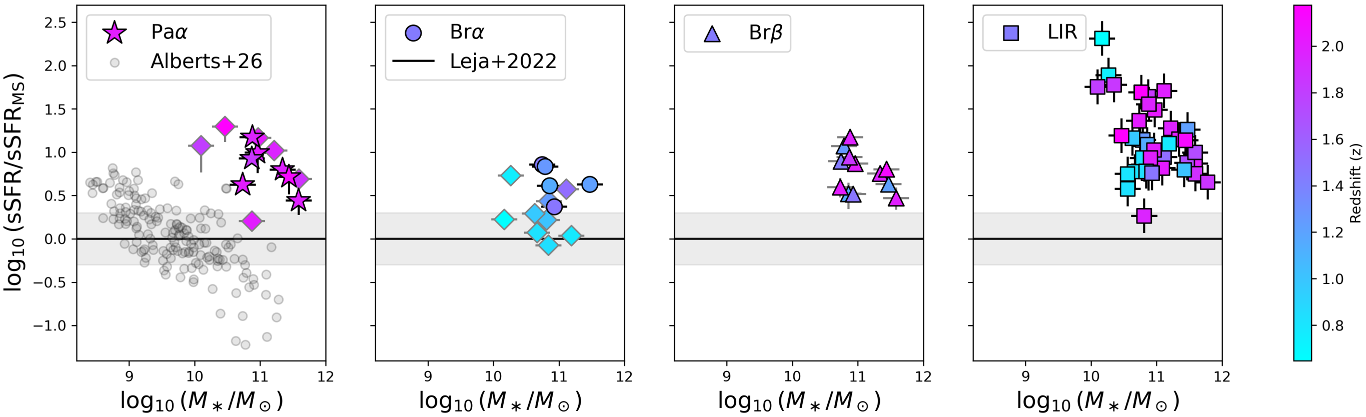

Figure 10. The ratio of each source's specific star formation rate ($\mathrm{sSFR} = \mathrm{SFR}/\mathrm{M}_\odot$) to the main-sequence from J. Leja et al. (2022) (solid line with $\pm 1\sigma$ scatter) vs. the stellar mass of each source. These star-formation rates are inferred from the dust corrected Paα (*Left* panel), Brα (*Second* panel), Brβ (*Third* panel), and $L_{\rm IR}$ (*Right* panel). Sources that had multiple hydrogen recombination lines to measure an individual attenuation have black outlines while the sources that used the mean attenuation for their dust correction are diamonds and have gray outlines. Star-formation rates from nebular lines follow closer to main sequence galaxies of similar mass and redshift, whereas $L_{\rm IR}$ SFR places our sources exclusively above the main-sequence as starburst galaxies.

et al. 2008; A. Kirkpatrick et al. 2015). Dust heating from old stars requires spectroscopy of features like the Balmer break to separate fully which future NIRSpec/PRISM observations may be able to provide. That being said, we see the greatest difference between $\mathrm{SFR_{IR}}$ and $\mathrm{SFR_{line}}$ among the lowest redshift subset ($z < 1$) with $f_{\rm AGN} < 30\%$ (Fig. 8), where dust heating by older stars might be the most pronounced in the most evolved galaxies of our sample with the least amount of AGN contamination. However, the contribution of dust heating from evolved stellar populations cannot be quantitatively constrained with the present data.

S. Alberts et al. (2026) calibrate photometric mid-IR SFR indicators using Paα with the FRESCO catalog as used in C. Neufeld et al. (2024), and discusses differences between $\mathrm{SFR_{IR}}$ and $\mathrm{SFR_{Pa\alpha}}$. Their work spans a larger stellar mass range that does not reach the massive starbursts represented in our sample (Fig. 6). Consequently, S. Alberts et al. (2026) infer $A_{\rm Pa\alpha} < 0.2$ mag from Hα/Paα ratios, which is also significantly less than what we find in our sample. The most massive starbursts at cosmic noon are significantly more attenuated than their main-sequence counterparts (E. da Cunha et al. 2008; J. A. Hodge et al. 2013; C. M. Casey et al. 2014a; K. E. Whitaker et al. 2017). In this work we demonstrate that this holds into the near-IR where the attenuation can reach up to 4 mag of attenuation at Paα. In local LIRGs well above the $z \sim 0$ main-sequence, H. Inami et al. (2018) find that Brβ-derived SFRs agree well with the $L_{\rm IR}$ SFRs when using the opacity models from mid-IR continuum fitting, which similarly predict low attenuation into the mid-IR. Although, our sample probes more extreme, dust-obscured systems than local LIRGs (e.g., A. Kirkpatrick et al. 2017; J. McKinney et al. 2023a). Compared to our $z \sim 1-2$ sample, the SFR tracer differences may arise from redshift evolution in galaxy gas mass fractions and dust-to-stellar mass fractions, whereby for fixed stellar mass star-forming galaxies with higher gas fractions increase the birth-cloud/mixed dust contrast (P. Santini et al. 2014; C. M. Casey et al. 2026b).

Figure 10 shows the position of our sample relative to the star-formation main sequence (SFMS) for each SFR diagnostic after correcting for attenuation. Since the galaxies in our sample are among the most luminous dust-obscured galaxies at $z \sim 1-2$, we expect them to fall above the SFMS (e.g., L. Yan et al. 2004; A. Kirkpatrick et al. 2015, 2017). Indeed, the 8 galaxies in the parent LRS sample with half-light radii from NIRCam (A. Genin et al. 2025) have SFR surface densities ($\Sigma\mathrm{SFR} \equiv \mathrm{SFR}/2\pi\mathrm{R_e^2}$) above the expected main-sequence range by ~ 0.5 dex (J. Nadolny et al. 2025). All sources where the attenuation is inferred directly from multiple recombination lines fall above the SFMS.

Some of the galaxies without multiple nebular lines, for which the average attenuation of the sample was assumed, overlap with the main sequence scatter (*First* and *Second* panel of Fig. 10). The attenuation we assume in these source could plausibly underestimate the true attenuation, and therefore underestimate the dust-corrected SFR. Additionally, the Brα sources, which are the least sensitive to dust attenuation, occupy the lower-redshift end of our sample, where the effects of dust heating by old stars may be more pronounced. We do not interpret the location of the Brα sources on the SFMS as evidence that the Brα SFRs are intrinsically more accurate, particularly because they show the largest $\mathrm{SFR}_{\mathrm{line}}$ and $\mathrm{SFR}_{\mathrm{IR}}$ discrepancies (Figure 8). With the aforementioned caveats in mind, this could also be attributed to a past (> 10 Myr) burst boosting the ~ 100 Myr-averaged $\mathrm{SFR}_{\mathrm{IR}}$ while the ~ 10 Myr-averaged SFR from Brα traces the time post-burst, reflecting either a declining or constant star-formation history. Medium band photometry or NIRSpec/PRISM spectra could be used to disentangle the competing effects of old stellar heating and declining star-formation histories as in O. R. Cooper et al. (2025).

5. CONCLUSIONS

In this work we select a sample of Paα, Brα, and Brβ-detected galaxies from an original sample of 37 LIRGs at $z \sim 1-2$ with spectra from JWST MIRI/LRS and Spitzer IRS. We then compare dust corrected hydrogen recombination line SFRs with their corresponding L_{IR} SFRs to study the effects of dust attenuation in the near-IR and SFR indicators out to $z \sim 2$. Our main conclusions are as follows:

- Using multiple Paschen and Brackett emission lines, we derive attenuation between $1.87-4.05\,\mu$m which can be as high as $A_\lambda = 4$ mag at $1.87\,\mu$m. We find that the IR continuum attenuation derived from J. McKinney et al. (2026) is insufficient to correct for the amount of nebular attenuation that we measure, consistent with the differential reddening between optical continuum and optical nebular lines found in other surveys of optical recombination lines.

- The dust-corrected near-IR recombination-line SFRs are systematically lower than $\mathrm{SFR}_{\mathrm{IR}}$ with an offset of a factor of ~ 2.5 on-average and up to an order of magnitude. We consider a variety of potential explanations including clumpy star-formation morphologies, declining or constant star-formation histories with a past burst, underestimated nebular reddening, and biased L_{IR} SFRs from AGN and/or old stars. We disfavor the AGN heating scenario due to our ability to measure and subtract the AGN contribution to far-IR dust emission.

- We present the first sample of Brα-derived SFRs in $z \sim 1$ LIRGs, with varying degrees of AGN contribution constrained by mid-IR spectroscopy out to $\sim 24\,\mu$m. Relative to Paα and Brβ, the Brα SFRs exhibit the greatest discrepancy with IR-derived SFRs while being the least sensitive to dust.

It is evident that in the most massive, dust-obscured galaxies around cosmic noon the effects of dust attenuation are significant out to $\lambda_{\mathrm{rest}} \sim 4\,\mu$m. Future observations using JWST NIRCam/grism and/or NIRSpec PRISM are needed to definitely characterize near-IR nebular line SFRs in dust-obscured cosmic noon starbursts. In particular, resolved Paα morphologies could constrain the effects of clumpy morphologies, while PRISM spectroscopy would provide a handle on dust heating from evolved stellar populations via the Balmer Break strength, and greatly improved star-formation history modeling.

ACKNOWLEDGMENTS

The data were obtained from the Mikulski Archive for Space Telescopes at the Space Telescope Science Institute, which is operated by the Association of Universities for Research in Astronomy, Inc., under NASA contract NAS 5-03127 for JWST. These observations are associated with program #3224. Support for program #3224 was provided by NASA through a grant from the Space Telescope Science Institute, which is operated by the Association of Universities for Research in Astronomy, Inc., under NASA contract NAS 5-03127.

V.V. acknowledges support for the Galaxy Evolution Vertically Integrated Project (GEVIP) undergraduate research group from the National Science Foundation under NSF-AAG-1908817 and NSF-AAG-2009905.

V.V. would like to thank the mentorship of J.M., S.F, and A.T. during her undergraduate career as well as the astronomy department at the University of Texas at Austin for the great amounts of support they provide to undergraduates interested in research. V.V. would also like to thank her husband, her parents, and her family for their constant support.

AUTHOR CONTRIBUTIONS

V.V. was responsible for the formal analysis, investigation, methodology, software, validation, visualization, writing the original draft, editing, and implementing suggested comments.

J.M. came up with the initial research concept, provided supervision and mentorship throughout the project, and reviewed and edited the draft throughout the writing process.

A.P. and A.S. were responsible for the conceptualization and expansion of the research as well as providing meaningful feedback.

All other authors provided helpful feedback.

Table 2. Recombination Line Luminosities and Derived Star Formation Rates. $f_{\rm AGN}$ denotes the AGN fractional contribution to the mid-IR. Stellar masses are derived from SED fitting by CIGALE. SFRs are measured using `emcee` as described in 3.2 with units of $M_\odot$ yr^{-1}, and have been corrected for dust attenuation as described in Section 3.3.

ID	$z_{\rm spec}$	$f_{\rm AGN}$ (%)	M_* ($M_\odot$)	SFR$_{\rm Pa\alpha}$	SFR$_{\rm Br\beta}$	SFR$_{\rm Br\alpha}$	SFR$_{\rm IR}$
FLS-IRS-8493	0.647	35	10.2 ±0.2	–	–	7^{+1}_{-1}	854 ± 393
FLS-IRS-8040	0.753	38	10.3 ±0.2	–	< 1460	32^{+5}_{-6}	459 ± 211
GN-IRS-27	0.776	35	11.2 ±0.2	< 159	< 1194	16^{+3}_{-3}	183 ± 84
GN-IRS-50	0.822	0	10.7 ±0.2	–	–	14^{+3}_{-3}	71 ± 33
GN-IRS-61	0.842	0	10.8 ±0.2	–	–	11^{+3}_{-2}	82 ± 38
GN-IRS-42	0.971	18	10.6 ±0.2	–	< 2990	29^{+6}_{-5}	214 ± 99
GN-IRS-6	1.009	0	10.8 ±0.2	–	–	< 922	126 ± 58
GN-IRS-5	1.150	0	10.9 ±0.2	–	73^{+25}_{-25}	< 1244	270 ± 124
GN-IRS-26	1.220	2	11.5 ±0.2	–	156^{+31}_{-29}	< 1701	663 ± 305
GN-IRS-2	1.242	0	10.8 ±0.2	–	< 2084	68^{+13}_{-12}	214 ± 99
GN-IRS-4	1.264	16	10.8 ±0.2	–	< 1153	< 1049	340 ± 157
GN-IRS-1	1.436	19	10.7 ±0.2	–	229^{+47}_{-44}	< 1017	409 ± 188
GN-IRS-63	1.466	9	10.9 ±0.2	–	112^{+22}_{-20}	80^{+13}_{-14}	196 ± 90
GN-IRS-3	1.515	0	11.1 ±0.2	–	< 3898	152^{+31}_{-27}	356 ± 164
FLS-IRS-22722	1.802	77	10.1 ±0.2	132^{+18}_{-67}	–	–	633 ± 292
FLS-IRS-289	1.844	37	10.9 ±0.2	386^{+45}_{-43}	< 7517	–	2002 ± 922
GN-IRS-19	1.886	63	11.6 ±0.2	364^{+44}_{-40}	< 644	–	418 ± 193
GN-IRS-15	1.962	22	11.2 ±0.2	637^{+72}_{-66}	–	–	1152 ± 531
FLS-IRS-22530	1.963	21	10.9 ±0.2	741^{+74}_{-74}	741^{+151}_{-132}	–	1784 ± 822
GN-IRS-21	1.974	47	11.3 ±0.2	417^{+45}_{-50}	377^{+72}_{-69}	< 2063	936 ± 431
GN-IRS-11	1.989	23	11.6 ±0.2	214^{+52}_{-68}	< 1224	< 3516	577 ± 266
GN-IRS-7	1.998	0	11.0 ±0.2	526^{+59}_{-220}	< 2397	< 5496	564 ± 260
GN-IRS-58	1.999	32	10.9 ±0.2	81^{+10}_{-9}	–	–	289 ± 133
GN-IRS-12	2.009	79	10.7 ±0.2	179^{+22}_{-24}	168^{+46}_{-40}	< 3373	980 ± 452
FLS-IRS-521	2.017	40	11.0 ±0.2	792^{+80}_{-74}	–	–	1665 ± 767
FLS-IRS-8226	2.119	69	11.4 ±0.2	388^{+48}_{-144}	475^{+110}_{-85}	< 2987	1027 ± 473
FLS-IRS-509	2.177	77	10.5 ±0.2	546^{+75}_{-185}	< 830	< 729	428 ± 197

REFERENCES

Alberts, S., Rieke, G. H., Shivaei, I., et al. 2026, arXiv e-prints, arXiv:2604.01326, doi: 10.48550/arXiv.2604.01326

Alonso-Herrero, A., Rieke, G. H., Rieke, M. J., et al. 2006, ApJ, 650, 835, doi: 10.1086/506958

Armus, L., Charmandaris, V., Bernard-Salas, J., et al. 2007, ApJ, 656, 148, doi: 10.1086/510107

Astropy Collaboration. 2026, FluxConservingResampler, https://specutils.readthedocs.io/en/stable/api/specutils.manipulation.FluxConservingResampler.html

Bardati, J., Hopkins, P. F., & Faucher-Giguère, C.-A. 2026, arXiv e-prints, arXiv:2603.12328, doi: 10.48550/arXiv.2603.12328

Baron, D., Sandstrom, K. M., Sutter, J., et al. 2025, ApJ, 978, 135, doi: 10.3847/1538-4357/ad972a

Beck, S. C., Ho, P. T. P., & Turner, J. L. 1989, in Infrared Spectroscopy in Astronomy, ed. E. Böhm-Vitense, 473

Birkin, J. E., Puglisi, A., Swinbank, A. M., et al. 2024, MNRAS, 531, 61, doi: 10.1093/mnras/stae1089

Boquien, M., Burgarella, D., Roehlly, Y., et al. 2019, A&A, 622, A103, doi: 10.1051/0004-6361/201834156

Bushouse, H., Eisenhamer, J., Dencheva, N., et al. 2025, JWST Calibration Pipeline, 1.17.1 Zenodo, doi: 10.5281/zenodo.14597407

Calzetti, D. 2013, in Secular Evolution of Galaxies, ed. J. Falcón-Barroso & J. H. Knapen, 419, doi: 10.48550/arXiv.1208.2997

Calzetti, D., Armus, L., Bohlin, R. C., et al. 2000, ApJ, 533, 682, doi: 10.1086/308692

Calzetti, D., Kennicutt, R. C., Engelbracht, C. W., et al. 2007, ApJ, 666, 870, doi: 10.1086/520082

Cardelli, J. A., Clayton, G. C., & Mathis, J. S. 1989, ApJ, 345, 245, doi: 10.1086/167900

Casey, C. M., Narayanan, D., & Cooray, A. 2014a, PhR, 541, 45, doi: 10.1016/j.physrep.2014.02.009

Casey, C. M., Berta, S., Béthermin, M., et al. 2012, ApJ, 761, 140, doi: 10.1088/0004-637X/761/2/140

Casey, C. M., Scoville, N. Z., Sanders, D. B., et al. 2014b, ApJ, 796, 95, doi: 10.1088/0004-637X/796/2/95

Casey, C. M., Akins, H. B., Battisti, A. J., et al. 2026a, arXiv e-prints, arXiv:2606.17270, doi: 10.48550/arXiv.2606.17270

Casey, C. M., Akins, H. B., Battisti, A. J., et al. 2026b, arXiv e-prints, arXiv:2606.17270, doi: 10.48550/arXiv.2606.17270

Chabrier, G. 2003, PASP, 115, 763, doi: 10.1086/376392

Charlot, S., & Fall, S. M. 2000, ApJ, 539, 718, doi: 10.1086/309250

Clarke, L., Shapley, A. E., Lam, N., et al. 2025, arXiv e-prints, arXiv:2510.06681, doi: 10.48550/arXiv.2510.06681

Cleri, N. J., Trump, J. R., Backhaus, B. E., et al. 2022, ApJ, 929, 3, doi: 10.3847/1538-4357/ac5a4c

Cooper, O. R., Brammer, G., Heintz, K. E., et al. 2025, ApJ, 982, 125, doi: 10.3847/1538-4357/adb8e1

da Cunha, E., Charlot, S., & Elbaz, D. 2008, MNRAS, 388, 1595, doi: 10.1111/j.1365-2966.2008.13535.x

Dannerbauer, H., Rigopoulou, D., Lutz, D., et al. 2005, A&A, 441, 999, doi: 10.1051/0004-6361:20052812

Davé, R., Anglés-Alcázar, D., Narayanan, D., et al. 2019, MNRAS, 486, 2827, doi: 10.1093/mnras/stz937

Depoy, D. L., Becklin, E. E., & Geballe, T. R. 1987, ApJL, 316, L63, doi: 10.1086/184893

Dong, X. Y., & Wu, X.-B. 2016, ApJ, 824, 70, doi: 10.3847/0004-637X/824/2/70

Dopita, M. A., Groves, B. A., Sutherland, R. S., & Kewley, L. J. 2003, ApJ, 583, 727, doi: 10.1086/345448

Draine, B. T. 2003, ARA&A, 41, 241, doi: 10.1146/annurev.astro.41.011802.094840

Ellison, S. L., Teimoorinia, H., Rosario, D. J., & Mendel, J. T. 2016, MNRAS, 458, L34, doi: 10.1093/mnrasl/slw012

Foreman-Mackey, D., Conley, A., Meierjurgen Farr, W., et al. 2013, emcee: The MCMC Hammer,, Astrophysics Source Code Library, record ascl:1303.002 http://ascl.net/1303.002

Gatto, L., Storchi-Bergmann, T., Riffel, R. A., et al. 2025, MNRAS, 539, 3229, doi: 10.1093/mnras/staf669

Genin, A., Shuntov, M., Brammer, G., et al. 2025, DAWN JWST Archive: Morphology from profile fitting of over 340000 galaxies in major JWST fields. Morphology evolution with redshift and galaxy type.,, 2025A&A...699A.343G

Gosling, A. J., Bandyopadhyay, R. M., & Blundell, K. M. 2009, MNRAS, 394, 2247, doi: 10.1111/j.1365-2966.2009.14493.x

Goyal, C., Ponnada, S. B., Hopkins, P. F., et al. 2026, PASP, 138, 034102, doi: 10.1088/1538-3873/ae4a4c

Granato, G. L., Lacey, C. G., Silva, L., et al. 2000, ApJ, 542, 710, doi: 10.1086/317032

Hayward, C. C., Lanz, L., Ashby, M. L. N., et al. 2014, MNRAS, 445, 1598, doi: 10.1093/mnras/stu1843

Heckman, T. M., & Best, P. N. 2014, ARA&A, 52, 589, doi: 10.1146/annurev-astro-081913-035722

Hickox, R. C., & Alexander, D. M. 2018, ARA&A, 56, 625, doi: 10.1146/annurev-astro-081817-051803

Hodge, J. A., Karim, A., Smail, I., et al. 2013, ApJ, 768, 91, doi: 10.1088/0004-637X/768/1/91

Hosek, Jr., M. W., Lu, J. R., Anderson, J., et al. 2018, ApJ, 855, 13, doi: 10.3847/1538-4357/aaabbb

Inami, H., Armus, L., Matsuhara, H., et al. 2018, A&A, 617, A130, doi: 10.1051/0004-6361/201833053

Inoue, A. K. 2001, AJ, 122, 1788, doi: 10.1086/323095

Karthikeyan, S., Clarke, L., Shapley, A. E., et al. 2026, arXiv e-prints, arXiv:2603.11338, doi: 10.48550/arXiv.2603.11338

Kennicutt, R. C., & Evans, N. J. 2012, ARA&A, 50, 531, doi: 10.1146/annurev-astro-081811-125610

Kennicutt, Jr., R. C. 1998, ARA&A, 36, 189, doi: 10.1146/annurev.astro.36.1.189

Kim, S. J., Goto, T., Ling, C.-T., et al. 2024, MNRAS, 527, 5525, doi: 10.1093/mnras/stad3499

Kirkpatrick, A., Pope, A., Sajina, A., et al. 2015, ApJ, 814, 9, doi: 10.1088/0004-637X/814/1/9

Kirkpatrick, A., Pope, A., Alexander, D. M., et al. 2012, ApJ, 759, 139, doi: 10.1088/0004-637X/759/2/139

Kirkpatrick, A., Pope, A., Sajina, A., et al. 2017, ApJ, 843, 71, doi: 10.3847/1538-4357/aa76dc

Krolik, J. H., & Vrtilek, J. M. 1984, ApJ, 279, 521, doi: 10.1086/161916

Lai, T. S. Y., Smith, J. D. T., Baba, S., Spoon, H. W. W., & Imanishi, M. 2020, ApJ, 905, 55, doi: 10.3847/1538-4357/abc002

Leitherer, C. 1990, ApJS, 73, 1, doi: 10.1086/191438

Leja, J., Speagle, J. S., Ting, Y.-S., et al. 2022, ApJ, 936, 165, doi: 10.3847/1538-4357/ac887d

Lo Faro, B., Buat, V., Roehlly, Y., et al. 2017, MNRAS, 472, 1372, doi: 10.1093/mnras/stx1901

Madau, P., & Dickinson, M. 2014, ARA&A, 52, 415, doi: 10.1146/annurev-astro-081811-125615

Man, A., & Belli, S. 2018, Nature Astronomy, 2, 695, doi: 10.1038/s41550-018-0558-1

Markov, V., Gallerani, S., Pallottini, A., et al. 2025, A&A, 702, A33, doi: 10.1051/0004-6361/202555182

Mathis, J. S. 1990, ARA&A, 28, 37, doi: 10.1146/annurev.aa.28.090190.000345

McKinney, J., Hayward, C. C., Rosenthal, L. J., et al. 2021, ApJ, 921, 55, doi: 10.3847/1538-4357/ac185f

McKinney, J., Pope, A., Armus, L., et al. 2020, ApJ, 892, 119, doi: 10.3847/1538-4357/ab77b9

McKinney, J., Pope, A., Kirkpatrick, A., et al. 2023a, ApJ, 955, 136, doi: 10.3847/1538-4357/ace25c

McKinney, J., Pope, A., Sajina, A., et al. 2023b, Measuring Dust Evolution Over the Past 10 Billion Years With 3-12 micron Spectra for 60 High-Redshift Galaxies,, JWST Proposal. Cycle 2, ID. #3224

McKinney, J., Eleazer, M., Pope, A., et al. 2026, ApJ, 1001, 93, doi: 10.3847/1538-4357/ae4d46

Mulcahey, C. R., Leslie, S. K., Jackson, T. M., et al. 2022, A&A, 665, A144, doi: 10.1051/0004-6361/202142215

Murphy, E. J., Chary, R.-R., Dickinson, M., et al. 2011, ApJ, 732, 126, doi: 10.1088/0004-637X/732/2/126

Murphy, Jr., T. W., Soifer, B. T., Matthews, K., Armus, L., & Kiger, J. R. 2001, AJ, 121, 97, doi: 10.1086/318031

Nadolny, J., Michałowski, M. J., Parente, M., et al. 2025, A&A, 693, L6, doi: 10.1051/0004-6361/202452794

Neufeld, C., van Dokkum, P., Asali, Y., et al. 2024, ApJ, 972, 156, doi: 10.3847/1538-4357/ad6158

Noeske, K. G., Weiner, B. J., Faber, S. M., et al. 2007, ApJL, 660, L43, doi: 10.1086/517926

Noll, S., Burgarella, D., Giovannoli, E., et al. 2009, A&A, 507, 1793, doi: 10.1051/0004-6361/200912497

Oesch, P. A., Brammer, G., Naidu, R. P., et al. 2023, MNRAS, 525, 2864, doi: 10.1093/mnras/stad2411

Oke, J. B. 1974, ApJS, 27, 21, doi: 10.1086/190287

Osterbrock, D. E., & Ferland, G. J. 2006, Astrophysics of gaseous nebulae and active galactic nuclei

Pope, A., Chary, R.-R., Alexander, D. M., et al. 2008, ApJ, 675, 1171, doi: 10.1086/527030

Popesso, P. 2023, in A Journey Through Galactic Environments: From the Halo Assembly Bias to the Satellite Quenching (galacticjourney2023), 7, doi: 10.5281/zenodo.10006928

Porras-Valverde, A. J., Ricarte, A., Natarajan, P., et al. 2026, ApJ, 998, 48, doi: 10.3847/1538-4357/ae2fb1

Prescott, M. K. M., Finlator, K. M., Cleri, N. J., Trump, J. R., & Papovich, C. 2022, ApJ, 928, 71, doi: 10.3847/1538-4357/ac5459

Reddy, N. A., Topping, M. W., Sanders, R. L., Shapley, A. E., & Brammer, G. 2023, ApJ, 948, 83, doi: 10.3847/1538-4357/acc869

Reddy, N. A., Shapley, A. E., Kriek, M., et al. 2020, ApJ, 902, 123, doi: 10.3847/1538-4357/abb674

Reddy, N. A., Shapley, A. E., Sanders, R. L., et al. 2026, ApJ, 999, 15, doi: 10.3847/1538-4357/ae38da

Retzlaff, J., Rosati, P., Dickinson, M., et al. 2010, A&A, 511, A50, doi: 10.1051/0004-6361/200912940

Rigby, J. R., & Rieke, G. H. 2004, ApJ, 606, 237, doi: 10.1086/382776

Runburg, J., Farrah, D., Sajina, A., et al. 2022, ApJ, 924, 133, doi: 10.3847/1538-4357/ac37b8

Sajina, A., Lacy, M., & Pope, A. 2022, Universe, 8, 356, doi: 10.3390/universe8070356

Sajina, A., Yan, L., Fadda, D., Dasyra, K., & Huynh, M. 2012, ApJ, 757, 13, doi: 10.1088/0004-637X/757/1/13

Sajina, A., Yan, L., Spoon, H., & Fadda, D. 2009, in Astronomical Society of the Pacific Conference Series, Vol. 408, The Starburst-AGN Connection, ed. W. Wang, Z. Yang, Z. Luo, & Z. Chen, 417, doi: 10.48550/arXiv.0901.4284

Sanders, R. L., Shapley, A. E., Topping, M. W., et al. 2025, ApJ, 989, 209, doi: 10.3847/1538-4357/adf066

Santini, P., Maiolino, R., Magnelli, B., et al. 2014, A&A, 562, A30, doi: 10.1051/0004-6361/201322835

Smith, J. D. T., Draine, B. T., Dale, D. A., et al. 2007, ApJ, 656, 770, doi: 10.1086/510549

Speagle, J. S., Steinhardt, C. L., Capak, P. L., & Silverman, J. D. 2014, ApJS, 214, 15, doi: 10.1088/0067-0049/214/2/15

Stalevski, M., Ricci, C., Ueda, Y., et al. 2016, MNRAS, 458, 2288, doi: 10.1093/mnras/stw444

Stanway, E. R., & Eldridge, J. J. 2019, A&A, 621, A105, doi: 10.1051/0004-6361/201834359

Stierwalt, S., Armus, L., Charmandaris, V., et al. 2014, ApJ, 790, 124, doi: 10.1088/0004-637X/790/2/124

Stone, M., Pope, A., McKinney, J., et al. 2022, ApJ, 934, 27, doi: 10.3847/1538-4357/ac778b

Tielens, A. G. G. M. 2008, ARA&A, 46, 289, doi: 10.1146/annurev.astro.46.060407.145211

Wang, S., & Chen, X. 2019, ApJ, 877, 116, doi: 10.3847/1538-4357/ab1c61

Weingartner, J. C., & Draine, B. T. 2001, ApJ, 563, 842, doi: 10.1086/324035

Weller, E. J., Pacucci, F., Ni, Y., Hernquist, L., & Park, M. 2025, ApJ, 979, 181, doi: 10.3847/1538-4357/ada360

Whitaker, K. E., Pope, A., Cybulski, R., et al. 2017, ApJ, 850, 208, doi: 10.3847/1538-4357/aa94ce

Whitaker, K. E., van Dokkum, P. G., Brammer, G., & Franx, M. 2012, ApJL, 754, L29, doi: 10.1088/2041-8205/754/2/L29

Wild, V., Asari, N. V., Rowlands, K., et al. 2025, The Open Journal of Astrophysics, 8, 3, doi: 10.33232/001c.128125

Woodrum, C., Shivaei, I., Witstok, J., et al. 2025, arXiv e-prints, arXiv:2510.00235, doi: 10.48550/arXiv.2510.00235

Wozniak, M. A., Reddy, N. A., Oesch, P. A., et al. 2026, arXiv e-prints, arXiv:2602.21329, doi: 10.48550/arXiv.2602.21329

Yan, L., Choi, P. I., Fadda, D., et al. 2004, ApJS, 154, 75, doi: 10.1086/422917

Zavala, J. A., Casey, C. M., Manning, S. M., et al. 2021, ApJ, 909, 165, doi: 10.3847/1538-4357/abdb27